ChemComm

Understanding Electrochemical Cation Insertion into Prussian Blue from Electrode Deformation and Mass Changes

Journal:	*ChemComm*
Manuscript ID	CC-COM-03-2021-001681.R1
Article Type:	Communication

COMMUNICATION

Understanding Electrochemical Cation Insertion into Prussian Blue from Electrode Deformation and Mass Changes

Received 00th January 20xx,
Accepted 00th January 20xx

DOI: 10.1039/x0xx00000x

Saeed Saeed,[a] Shelby Boyd,[a] Wan-Yu Tsai,[b] Ruocun Wang,[a] Nina Balke,[c] and Veronica Augustyn*[a]

Alkali ion insertion into Prussian blue from aqueous electrolytes is characterized with *operando* AFM and EQCM, showing coupling of current with deformation and mass change rates. Stable cycling occurs only with K^+, attributed to its lower hydration energy. The (de)insertion of K^+ results in reversible deformation even in the open framework structure.

Prussian blue and its analogs are 3D framework materials that undergo reversible ion insertion in aqueous and non-aqueous electrolytes. Due to their large interstitial sites (radius ~ 1.6 Å), these materials are flexible insertion hosts and of interest as electrodes for "beyond Li-ion" energy storage.[1-4] They are also candidates for emerging applications of ion insertion materials in desalination, ion separation, and element recovery.[5] The cubic structure of Prussian blue, $Fe_4[Fe(CN_6)]_3$, is shown in **Figure S1**a and highlights the interstitial sites occupied by A cations. The structure can also accommodate structural water and vacancy defects that impact the insertion behavior.[1]

It is hypothesized that the open framework of Prussian blue analogs allows for long cycle life and capacities of up to 170 mAh/g.[6] This performance is dependent on the nature of the electrolyte solvent and the cation. For example, in aqueous electrolytes, the potential for cation insertion into $Na_2Ni[Fe(CN)_6]$ increased linearly with alkali ion hydration energy.[7] There are also reported differences in the behavior of solvating water molecules during cation insertion: cations with larger ionic radii, such as K^+, tend to dehydrate during insertion, while smaller cations such as Li^+ enter with a hydration shell.[8,9] This occurs because alkali cation hydration energy is proportional to $1/r$ where r is the cation radius.[10] Therefore, we hypothesize that varying the aqueous electrolyte cation (and thus its tendency to dehydrate during insertion) should lead to differences in the electrochemical ion insertion-induced deformation of Prussian blue. The degree of structural change of the host is a critical factor in the cycling stability and kinetics of insertion materials.[11]

Recently, we developed an *operando* atomic force microscopy (AFM) technique to characterize the deformation of insertion-type electrode materials during electrochemical cycling.[12,13] Using this technique, we report the first *operando* AFM dilatometry measurements of Prussian blue for aqueous cation insertion, showing correlation between the local deformation rate obtained via AFM with the electrochemical current from the overall electrode. This allowed us to effectively measure the local electrochemomechanics associated with ion insertion. Here, we use this AFM technique along with electrochemical quartz crystal microbalance (EQCM) to understand the ion insertion-induced deformation of Prussian blue in aqueous electrolytes. We find that a lower cation hydration energy plays a critical role in determining the cycling stability of Prussian blue in aqueous electrolytes, with cyclability ranked as $K^+ > Na^+ > Li^+$. EQCM results indicate that K^+ inserts without its hydration shell. Nevertheless, *operando* AFM demonstrates that Prussian blue undergoes reversible deformation, which we hypothesize leads to capacity fade over time, even for the insertion of dehydrated K^+ into the fairly open framework. The structural deformation is intrinsically coupled to the insertion process, with the rate of deformation obtained from *operando* AFM and rate of mass change obtained from EQCM correlating with the electrochemical current.

Physical characterization of the electrodeposited Prussian blue is shown in **Fig. S1**b-d. Electrochemical cation insertion into Prussian blue in aqueous electrolytes can be described as:[14]

$$KFe^{3+}[Fe^{2+}(CN)_6] + xA^+ + xe^- \leftrightarrow A_xKFe^{3-x+}[Fe^{2+}(CN)_6] \quad (1)$$

where A^+ represents an alkali cation. The capacity associated with $x = 1$ is 87 mAh/g of $KFe[Fe(CN)_6]$ and occurs at a half-wave potential of 0.2 V vs. Ag/AgCl. Cyclic voltammetry at 10 mV/s shows one reversible redox couple in each of the electrolytes,

[a] *Department of Materials Science and Engineering, North Carolina State University, Raleigh, NC 27695.*
[b] *Chemical Science Division, Oak Ridge National Laboratory, Oak Ridge, Tennessee 37830.*
[c] *Center for Nanophase Materials Sciences, Oak Ridge National Laboratory, Oak Ridge, Tennessee 37830*
† * corresponding author, email: vaugust@ncsu.edu
Electronic Supplementary Information (ESI) available: Methods, Figures S1-S10. See DOI: 10.1039/x0xx00000x

attributed to cation (de)insertion (**Figure 1**a). The half-wave potential, $E_{1/2}$, shifts to lower potentials from K_2SO_4 to Na_2SO_4 to Li_2SO_4. The highest capacity is obtained in K_2SO_4 (50 mAh/g, 0.6 e^- per $KFe_2(CN)_6$), followed by Na_2SO_4 (37 mAh/g, 0.4 e^-), and finally Li_2SO_4 (24 mAh/g, 0.3 e^-). In addition to having the lowest capacity, cycling in Li_2SO_4 shows the poorest capacity retention and Coulombic efficiency (**Fig. 1**b). There are also differences in how the CVs change as a function of scan rate. Cyclic voltammograms (CVs) from 10 – 200 mV/s in 0.5 M K_2SO_4, Na_2SO_4, and Li_2SO_4 are shown in **Figure S3**a-c. In K_2SO_4, the redox peaks show increased current and peak-to-peak separation with increasing scan rates. Cation insertion is still present at 200 mV/s (**Fig. S3**a) and it is limited by solid state diffusion (*vide infra*). In Na_2SO_4 and especially Li_2SO_4, the redox peaks lose definition so that by 200 mV/s in Li_2SO_4, the CV appears capacitive. The current decreases with scan rate in Li_2SO_4. The insertion current decays significantly within just three cycles in Li_2SO_4 and Na_2SO_4 electrolytes, in contrast to the good cycling stability in K_2SO_4 (**Fig. S4**). These changes indicate that the poor cycling performance in the Li_2SO_4 and Na_2SO_4 electrolytes occurs due to progressive loss of Prussian blue from the substrate.

The capacity and cycling stability of Prussian blue decrease as a function of electrolyte cation, in the order $K^+ > Na^+ > Li^+$. This differs from the trend observed upon ion insertion from non-aqueous electrolytes, where the best cycling stability is obtained with Li^+.[15] In non-aqueous electrolytes, the cycling stability is primarily determined by the ion charge and radius, since the solvation energies of cations are low compared to those in aqueous electrolytes.[16] The trend in **Fig. 1** agrees with other reports on Prussian blue analogs in aqueous electrolytes.[17,18] While Prussian blue analogs have known dissolution issues in neutral-pH electrolytes,[19] the cation dependence suggests that hydration energy also plays a role. As

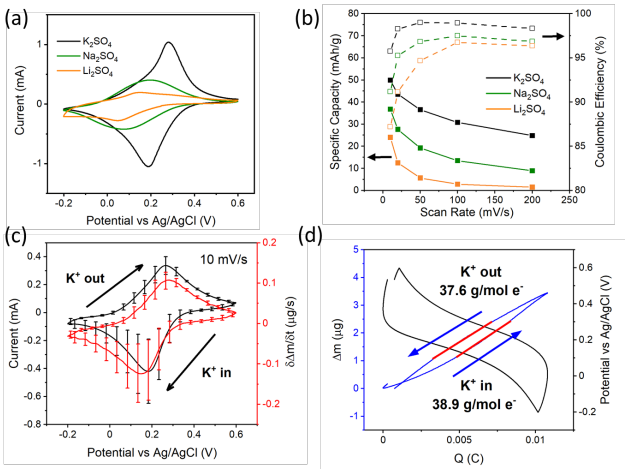

Figure 1 Electrochemical cation insertion into Prussian blue from different aqueous electrolytes. a) CVs in 0.5 M K_2SO_4, Na_2SO_4, and Li_2SO_4 at 10 mV/s. b) Cathodic capacity and Coulombic efficiency as a function of scan rate for all three electrolytes. c) Negative rate of mass change ($-\delta\Delta m/\delta t$) overlaid with a CV of Prussian blue at 10 mV/s in 0.5 M K_2SO_4 from EQCM. d) Determination of the mass-to-charge ratio (m/Q) from EQCM measurement of Prussian blue cycled in 0.5 M K_2SO_4 at 10 mV/s.

shown in **Table S1**, K^+ has the biggest ionic radius (1.37 Å) while Li^+ has the biggest hydrated radius (2.37 Å). It has been proposed that Prussian blue exhibits ion specificity based on size due to the 1.6 Å-radius of the channel connecting the A-sites.[20] The hydration energy of the inserting cation increases in the order $Li^+ > Na^+ > K^+$, which is opposite to the electrochemical stability of the films. This suggests that cycling stability is affected by the high hydration energy of Li^+, which causes it to insert with a hydration shell, and subsequently leads to significant structural deformation and eventual film delamination or dissolution. To confirm this hypothesis, we performed SEM and energy dispersive X-ray spectroscopy (EDS) at the interface of an electrochemically cycled and uncycled electrode region in Li_2SO_4 (**Figure S5**a - g). In the cycled region, the decrease in potassium, iron, and nitrogen shows that these elements, and thus Prussian blue, have been removed from the electrode, consistent with the loss of current shown by cyclic voltammetry in Li_2SO_4. Due to its lower hydration energy, K^+ sheds its solvation shell and inserts without water molecules. To confirm the dehydration of K^+ and understand the electrode deformation dynamics, we performed EQCM and *operando* AFM, respectively.

EQCM was used to determine the nature of the inserting species in 0.5 M K_2SO_4. The change in mass (Δm) vs. potential is shown in **Figure S6**. The electrode mass increases upon cathodic polarization, consistent with a cation insertion mechanism. At scan rates > 20 mV/s, increased electrode polarization leads to more sluggish cation (de)insertion. This is shown by the continued anodic current / decrease in Δm upon scan rate reversal at the anodic vertex potential (0.6 V) and continued cathodic current / increase in Δm at the cathodic vertex potential (-0.2 V). As shown in **Fig. 1**c and **Figure S7**, there is close coupling between the rate of mass change ($-\delta\Delta m/\delta t$) and electrochemical current. The electrochemical current (i.e. the capacity rate) can be related to the first derivative of the frequency (mass) change with respect to time.[21] As a result, plots of $-\delta\Delta m/\delta t$ are qualitatively similar to the CVs. To determine the inserting species, we calculated the mass-to-charge ratio (m/Q; **Fig. 1**d). It is 38.9 g/mol e^- in the cathodic region and 37.6 g/mol e^- in the anodic region. This is in agreement with K^+ insertion into Prussian blue without coordinating water, which corresponds to a theoretical m/Q of 39.098 g/mol e^-. As the scan rate increases, the mass-to-charge ratios show some variation, but are near values for K^+ insertion. However, the CVs become more irreversible and the maximum Δm gradually decreases as less K^+ inserts into the electrode (**Figure S8**). The EQCM results demonstrate the loss of the K^+ hydration shell before insertion, which is in line with previous reports.[8,9,22,23]

Differences in the cycling stability as a function of electrolyte cation led us to consider the role of K^+ insertion on the deformation of Prussian blue. *Operando* AFM and EQCM measurements were attempted in Li_2SO_4 and Na_2SO_4 electrolytes, however, the films degraded too rapidly during electrochemical cycling. **Figure 2**a and b, respectively, show the deformation and deformation rate of Prussian blue obtained from *operando* AFM dilatometry in 0.5 M K_2SO_4. The

deformation rate exhibits a similar relationship with potential as the current, resulting in curves almost identical to the CVs (**Figure S9**a-d). We define these curves "mechanical" CVs, or "mCVs." This direct correlation occurs due to the coupling between deformation (δ) and total charge (Q) that arises because the insertion of a guest into the host typically requires a volume change.[11,24,25] As a result, their rates (deformation rate and current) are also directly related. In Prussian blue, the maximum deformation rate occurs at the peak cathodic and anodic current. The (de)insertion of K^+ results in a reversible volume change that is centered around the redox peaks. It is consistent with prior *in situ* and *ex situ* XRD reports that showed changes in the lattice parameter of Prussian blue and related analogs during cation insertion.[6,26,27] Cycling in K_2SO_4 resulted in slight degradation of the film as observed via AFM (**Figure S10**), which may be due to the aforementioned dissolution during cycling at neutral pH. A 5 × 5 grid mCV map was performed across a 5 μm × 5 μm area (**Fig. S10**a-c). In these experiments, the current signal was from the whole electrode (global) and the deformation was from the area in contact with the AFM probe (local). Comparison of the 2D histograms of the CV and mCV shows slight film degradation on both the global and local scale (**Fig. S10**d-e).

To further understand the kinetics associated with K^+ (de)insertion and the associated Prussian blue deformation, we tracked the behavior of the peak current and peak deformation rate with scan rate. In cyclic voltammetry, the relationship between current and scan rate can be expressed as:[28]

$$i(E) = av^b \quad (2)$$

where $i(E)$ is the current as a function of potential, a and b are constants, and v is the scan rate. The b-value ($0.5 \leq b \leq 1$) is determined by the rate-limiting mechanism of the system. A surface-limited current will give rise to a b-value of 1, while a semi-infinite diffusion limited current will have a b-value of 0.5. Here, we assume that diffusion of K^+ in the aqueous electrolyte is much faster than the diffusion of K^+ in Prussian blue, and therefore a $v^{0.5}$ dependence would indicate K^+ transport limited by solid state diffusion. The relationship between the peak current and scan rate (**Fig. 2**c) has a b-value of ~ 0.5, indicative of semi-infinite diffusion limitation in the solid. Since the CVs and mCVs appear qualitatively similar, we also determined the "b-value" of the deformation rate (**Fig. 2**d). The peak deformation rate has a higher b-value of 0.9 - 1, indicative of a surface-limited response. The difference in b-value between the peak deformation rate and current could arise from differences between local (AFM) and global (CV) measurements in the electrodeposited Prussian blue film. Since AFM is a local deformation measurement, thinner regions of the electrode may lead to a higher b-value. On the other hand, the CV measurement is a global response of the current from all regions of the electrode, both thick and thin. Alternatively, the dependence between electrode deformation and charge might not be linear. The exact origin of this behavior will be the subject of future studies.

Figure 3 summarizes the data for K^+ (de)insertion into Prussian blue from cyclic voltammetry, *operando* AFM, and EQCM at 10 mV/s, showing strong coupling between charge, electrode mass change, and electrode deformation (**Fig. 3**a-c) and their time derivatives (**Fig. 3**d-f). During K^+ de-insertion, the capacity (Q) decreases, as does the electrode mass (Δm). The changes in capacity and mass as a function of time (and potential) give rise to peaks in the current (**Fig. 3**d) and rate of mass change (**Fig. 3**e) plots. In terms of deformation (**Fig. 3**c), the electrode contracts (δ decreases) until approximately the anodic peak current, at which point the electrode begins to expand (δ increases). The corresponding deformation rate (**Fig. 3**f) shows multiple peaks and relatively constant deformation rate after the anodic peak current, during the expansion stage. This behavior may indicate the presence of a structural transformation in the Prussian blue. Previous studies have shown that Prussian blue can undergo structural transitions during electrochemical cycling.[4,14,29] During K^+ insertion, the behavior is reversed. Although the three techniques show similar trends, the agreement between EQCM and CV is closer than with AFM, which we attribute to differences between global vs. local characterization techniques and sensitivity of the AFM to phase changes through a change in electro-chemo-mechanical coupling coefficients. The AFM results present localized and additional features that could occur due to the heterogeneity of the insertion reaction on the thin film and will be the topic of future investigation.

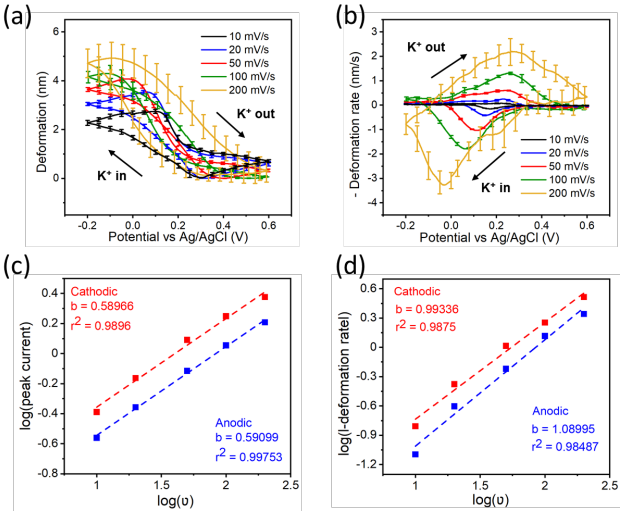

Figure 2 Kinetic analysis of current and deformation rate from *operando* AFM. (a) Average deformation vs. potential from 10 – 200 mV/s. (b) Average negative deformation rate vs. potential from 10 – 200 mV/s. Error bars indicate the standard deviation over 20 cycles. (c, d) b-value determination for the peak anodic and cathodic currents (c) and peak anodic and cathodic deformation rates (d).

In this study, we investigated cation insertion from aqueous electrolytes into Prussian blue with *operando* AFM and EQCM. Cyclic voltammetry showed that cycling stability was dependent on electrolyte cation, with $K^+ > Na^+ > Li^+$. SEM EDS showed that after electrochemical cycling in a Li_2SO_4 electrolyte, the Prussian blue film dissolved or delaminated. However, the film was retained upon cycling in a K_2SO_4 electrolyte, where the mass-to-charge ratios obtained from EQCM showed that charge storage

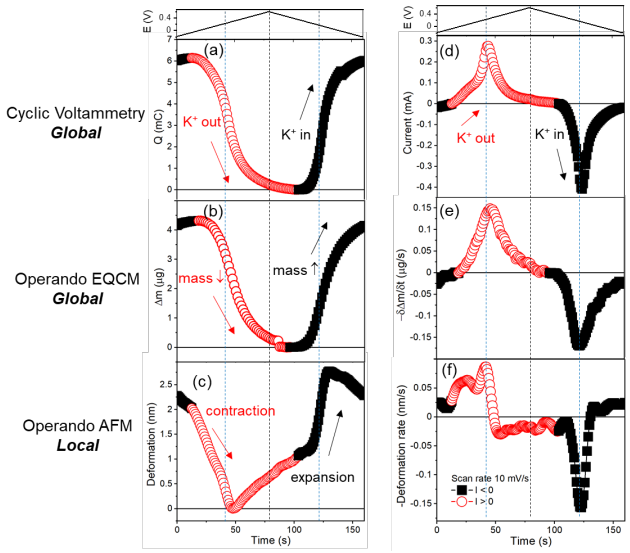

Figure 3 Comparison of K^+ (de)insertion into Prussian blue via electrochemistry (CV), EQCM, and AFM as a function of time at 10 mV/s. (a) Charge, (b) mass change, (c) deformation (expansion defined as $\delta > 0$), (d) current, (e) negative rate of mass change, and (f) negative deformation rate. Red indicates behavior during the anodic current, associated with K^+ de-insertion ("K^+ out."). The three vertical dashed lines indicate the peak anodic current, anodic turnover potential, and peak cathodic current.

occurred from K^+ insertion. *Operando* AFM in the same electrolyte showed reversible expansion and contraction upon K^+ (de)insertion. These results are consistent with the hypothesis that cycling stability of Prussian blue in aqueous electrolytes is higher for the insertion of cations with low hydration energies such as K^+ because they can shed their hydration shell during insertion. On the other hand, cations such as Li^+ enter with their large hydration shell, leading to rapid structural deterioration. Finally, we demonstrated the close coupling between rate of mass change (from EQCM), deformation rate (from *operando* AFM), and current (from cyclic voltammetry). Together, these techniques provide insight into the fundamental relationships between mechanical deformation and electrochemical insertion which can be applied to other insertion hosts.

Acknowledgements

This work was supported as part of the Fluid Interface Reactions, Structures and Transport, an Energy Frontier Research Center funded by the U.S. Department of Energy, Office of Science, Office of Basic Energy Sciences at Oak Ridge National Laboratory under contract #DE-AC0500OR22725 with UT Battelle, LLC. S.S. acknowledges a Hood Graduate Fellowship from NC State University. S.B. acknowledges a graduate fellowship from the NSF GRFP under Grant No. 571800. *Operando* AFM was conducted at the Center for Nanophase Materials Sciences, which is a DOE Office of Science User Facility. XRD, SEM, and EDS were performed at the Analytical Instrumentation Facility (AIF) at North Carolina State University (NCSU), which is supported by the State of North Carolina and the National Science Foundation (Grant ECCS-1542015).

References

1 X. Wu, J. J. Hong, W. Shin, L. Ma, T. Liu, X. Bi, Y. Yuan, Y. Qi, T. W. Surta, W. Huang, J. Neuefeind, T. Wu, P. A. Greaney, J. Lu and X. Ji, *Nat. Energy* 2019, **4**, 123–130.
2 M. Pasta, C. D. Wessells, N. Liu, J. Nelson, M. T. McDowell, R. A. Huggins, M. F. Toney and Y. Cui, *Nat. Commun.*, 2014, **5**, 3007.
3 J. Qian, C. Wu, Y. Cao, Z. Ma, Y. Huang and X. Ai, *Adv. Energy Mater.*, 2018, 1702619.
4 X. Guo, Z. Wang, Z. Deng, X. Li, B. Wang, X. Chen and S. P. Ong, *Chem. Mater.*, 2019, **31**, 5933–5942.
5 P. Srimuk, X. Su, J. Yoon, D. Aurbach and V. Presser, *Nat. Rev. Mater.*, 2020, **5**, 517–538.
6 Y. You, X. L. Wu, Y. X. Yin and Y. G. Guo, *Energy Environ. Sci.*, 2014, **7**, 1643–1647.
7 J. Yun, J. Pfisterer and A. S. Bandarenka, *Energy Environ. Sci.*, 2016, **9**, 955–961.
8 C. Gabrielli, J. J. Garcı and U. V. De Valencia, *J. Phys. Chem. B*, 2002, **106**, 3182–3191.
9 Y. Mizuno, M. Okubo, E. Hosono, T. Kudo, H. Zhou and K. Oh-ishi, *J. Phys. Chem. C*, 2013, **117**, 10877–10882.
10 G. Wulfsberg, in *Principles of Descriptive Inorganic Chemistry*, University Science Books, Sausalito, 1991, pp. 21–57.
11 V. Augustyn, R. Wang, N. Balke, M. Pharr and C. B. Arnold, *ACS Energy Lett.* 2020, **5**, 3548–3559.
12 R. Wang, J. B. Mitchell, Q. Gao, W. Tsai, S. Boyd, M. Pharr, N. Balke and V. Augustyn, *ACS Nano*, 2018, **12**, 6032–6039.
13 W. Tsai, R. Wang, S. Boyd, V. Augustyn and N. Balke, *Nano Energy*, 2021, **81**, 105592.
14 E. E. Levin, A. A. Kokin, D. E. Presnov, A. G. Borzenko, S. Y. Vassiliev, V. A. Nikitina and K. J. Stevenson, *ChemElectroChem*, 2020, 761–769.
15 Z. Shadike, D. Shi, M. Cao, S. Yang, J. Chen and Z. Fu, *R. Soc. Chem.*, 2017, **5**, 6393–6398.
16 B. Case and R. Parsons, *Trans. Faraday Soc.*, 1967, **63**, 1224–1239.
17 C. D. Wessells, S. V. Peddada, M. T. McDowell, R. A. Huggins and Y. Cui, *J. Electrochem. Soc.*, 2011, **159**, A98–A103.
18 S. Phadke, R. Mysyk and M. Anouti, *J. Energy Chem.*, 2020, **40**, 31-38.
19 T. Shao, C. Li, C. Liu, W. Deng, W. Wang, M. Xue and R. Li, *J. Mater. Chem. A* 2019, **7**, 1749–1755.
20 K. Itaya, I. Uchida and V. D. Neff, *Acc. Chem. Res.*, 1986, **19**, 162–168.
21 I. Rubinstein, *Physical Electrochemistry: Science and Technology,* Marcel Dekker, New York, 1995.
22 A. Shrivastava, S. Liu and K. C. Smith, *Phys. Chem. Chem. Phys.*, 2019, **21**, 20177–20188.
23 L. Chen, H. Shao, X. Zhou, G. Liu, J. Jiang and Z. Liu, *Nat. Commun.*, 2016, **7**, 11982.
24 A. Yu. Luchkin, Sergey; Romanyuk, Konstantin; Ivanov, Maxim; L. Kholkin, *J. Appl. Phys.*, 2015, 118.
25 F. Sauvage, L. Laffont, E. Baudrin, L. De Re and P. Na, *Inorg. Chem.*, 2007, **46**, 3289–3294.
26 T. Ikeshoji and T. Iwasaki, *Inorg. Chem.*, 1988, **27**, 1123–1124.
27 Y. You, X. Yu, Y. Yin, K. Nam and Y. Guo, *Nano Res.*, 2015, **8**, 117–128.
28 H. Lindström, S. Södergren, A. Solbrand, H. Rensmo, J. Hjelm, A. Hagfeldt and S.-E. Lindquist, *J. Phys. Chem. B*, 1997, **101**, 7717–7722.
29 W. R. Brant, R. Mogensen, S. Colbin, D. O. Ojwang, S. Schmid, L. Häggström, T. Ericsson, A. Jaworski, A. J. Pell and R. Younesi, *Chem. Mater.*, 2019, **31**, 7203–7211.